Article

Tuning the Magnetically Segregated Nanolayering in Mn−Ni−As Intermetallics

Bruno Gonano,* Øystein Slagtern Fjellvåg, Gwladys Steciuk, Francois Guillou, Dipankar Saha, Denis Pelloquin, and Helmer Fjellvåg*

Read Online

| ACCESS | | Metrics & More | | Article Recommendations | | Supporting Information |

ABSTRACT: 2D materials exhibiting alternating ferro- and non-ferromagnetic layers are highly sought due to their potential for applications. In this work, we demonstrate, through the use of robust methodology, the existence of single-phase, $Mn_{1−x}Ni_xAs$ ($0.25 \leq x \leq 0.50$), with a unique intrinsic nanostructuring where the thickness of MnAs and NiAs nanolayers can be tuned via the composition, x. We describe a periodic variation of nanolayers of edge-sharing $MnAs_6$ and $NiAs_6$ octahedra layers with thicknesses ranging from 1 to 6 octahedra, 2−16 Å. These crystalline structures are modulated and fully described based on 3D electron diffraction and neutron diffraction. Moreover, by X-ray magnetic circular dichroism, an elemental and orbital-specific technique, we probe the $3d$ magnetic moments of Mn and Ni. We unveil that the nanosegregated MnAs and NiAs layers behave very differently, with the magnetic moment of manganese being one order of magnitude greater than that of nickel. This study opens the path to a completely new class of materials with intrinsic layers of high and low magnetization with potential applications within spintronics.
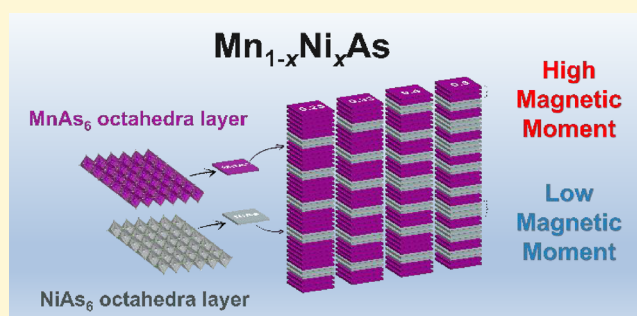
1. INTRODUCTION

The benefits of fundamental research as a guide toward applications and innovations are since long demonstrated by magnetic materials; however, the transfer process is still ongoing. $3d$-based intermetallic materials can be brought at the verge of stability between different magnetic, crystal, or electronic structures, leading in turn to unusual phase transitions potentially involving changes in local magnetic moments and discontinuities in magnetic, lattice, or electronic entropies. In this vast energy landscape, exotic properties such as magnetoresistance,[1−3] magnetocaloric effect,[4−8] and super-conductivity[9,10] arise, opening for potential applications. The physicochemical properties of these compounds are determined by the nature of chemical bonding, the crystal structure,[11] and especially the dimensionality[12] of the crystal structure, which has a major impact on the properties. In this perspective, low-dimensional (2D) materials present a scientific playground where the layering is inherent to the atomic arrangement and is consequently at the angstrom (Å) scale. The search for new magnetic phases exhibiting characteristic 2D properties is non-trivial and requires an interdisciplinary approach by chemistry and physics, at the cutting edge of materials science. 2D materials with magnetic layers are particularly interesting due to their strong magnetic anisotropy but also electronic anisotropy, leading to complex phenomena such as charge and spin density waves,[13−15] staircase-like magnetism,[16] magnetic exchange bias effect,[17] or

even superconductivity.[18,19] In addition to the fundamental interest, such 2D materials hold great potential for applications in, *e.g.*, data storage and spintronics.[20] Materials presenting an alternation of magnetic and non-magnetic layers may act as spin valves[21−24] or as magnetic tunnel junctions[25−28] and are currently widely exploited for MRAM[29,30] (magnetic random access memory). In this field, two-dimensional structures are desired but just very few crystalline materials display the structural features of stacked ferromagnetic and non-ferromagnetic layers with sufficient control of layer thickness and spacing. Therefore, such layered structures are today typically constructed by thin-film techniques[31] where one grows alternating layers of ferromagnetic (*e.g.*, CoFe, NiFe, or more recently the doped oxide Co-TiO$_2$)[32] and diamagnetic (*e.g.*, alumina Al_2O_3 is widely used) materials. Giant magneto-resistance is an exotic phenomenon that can occur in ferromagnetic and non-ferromagnetic multilayer structures.[33,34] Additionally, a strong magnetocaloric effect is predicted in ferromagnetic/paramagnetic multilayer structures.[35] However, even if thin-film techniques are well established, assembling
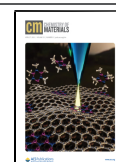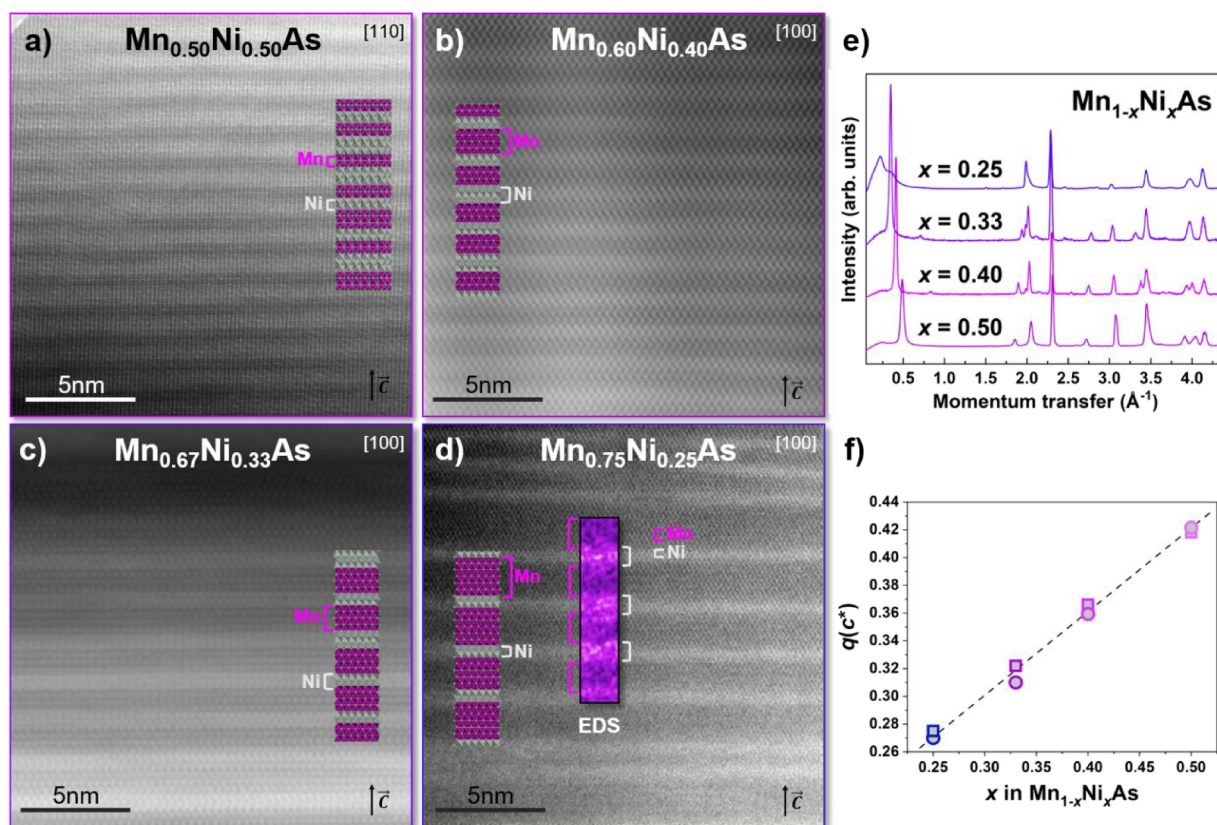
Figure 1. Experimental [110] and [100] HAADF (×12M) images of $Mn_{0.50}Ni_{0.50}As$, $Mn_{0.60}Ni_{0.40}As$, $Mn_{0.67}Ni_{0.33}As$, and $Mn_{0.75}Ni_{0.25}As$ (a, b, c, and d, respectively). Brighter and darker layers correspond to NiAs and MnAs layers, respectively. Structural models extracted from 3D ED are included. An EDX spectrum is shown in panel (d), evidencing richer Mn zones (purple) and Ni zones (gray). (e) Neutron powder diffraction patterns of $Mn_{0.50}Ni_{0.50}As$, $Mn_{0.60}Ni_{0.40}As$, $Mn_{0.67}Ni_{0.33}As$, and $Mn_{0.75}Ni_{0.25}As$ samples. (f) Variation of the modulation vector (q) vs x (circles: NPD/squares: 3D ED).

such complex structures can be challenging; thus, if a single compound could display the sought stacking of ferromagnetic and non-ferromagnetic layers, this will be of major importance for the field. The natural mineral hematite−ilmenite intergrowths present a rare example of a bulk compound displaying exotic nanolayers revealing a magnetic exchange bias, opening the way to potential applications.[17,36]

We recently unraveled an exotic nanoscale layering phenomenon in the intermetallic compound $Mn_{0.60}Ni_{0.40}As$,[37] described as a 2D ordering originating from an incommensurate occupational modulation of Mn and Ni, giving rise to alternating MnAs and NiAs layers of 2−4 unit cell in thickness. This periodic variation of ultrathin edge- and face-sharing $MnAs_6$ and $NiAs_6$ octahedra layers is completely different from any other stacking or order/disorder phenomena observed up to now. In bulk, binary MnAs is ferromagnetic and NiAs is Pauli paramagnetic. Hence, blending these at the nanoscale offers a pathway for a tunable alternation of layers with high and low magnetic moments. The very understanding of the connection between modulated composition and magnetic properties in $Mn_{1-x}Ni_xAs$ is therefore important and interesting.

2. EXPERIMENTAL AND METHODS SECTION

2.1. Synthesis. Samples were obtained by solid-state synthesis. First, MnAs and NiAs were prepared by carefully mixing Mn, Ni, and As elements, placed in alumina crucibles, and inserting them in silica quartz tubes, followed by heating for 3 weeks at 900 °C in a standing furnace (heating/cooling rate: 1 °C/min) with intermediate grind-

ings. Ternaries intermetallics samples were obtained by mixing stoichiometric amounts of MnAs and NiAs. The mixture was then placed in an alumina crucible, itself placed in a silica quartz tube. Tubes were then placed in standing furnaces. The heat treatment consists of three heating and cooling processes (heating/cooling rate: 1 °C/min) up to 800 °C with intermediate grindings. The sample was then annealed at 600 °C for 1 month. The last annealing is crucial to obtain the superstructure. We find the synthesis of the samples to be very reproducible, and the modulation vector is found to be the same across different sample batches.

2.2. Atomic Imaging. High-angle annular dark field (HAADF) imagery imaging was performed on an ARM 200F with a corrected probe, operating at 200 kV and equipped with a Centurio EDX spectrometer. The simulated ADF images were calculated with the JEMS software considering the convolution of a STEM probe with the intensity of the object (square of the projected potential multiplied by the electron−matter interaction constant of the structure).

2.3. 3D ED. For 3D electron diffraction (3D ED) analysis,[38,39] the $Mn_{1-x}Ni_xAs$ (x = 0.25, 0.33, 0.40, and 0.50) samples were crushed in a mortar with ethanol and deposited on a Cu grid with a thin film of holey amorphous carbon. 3D electron data (3D ED) data were collected with a FEI Tecnai G^2 20 transmission electron microscope (TEM) (acceleration voltage of 200 kV, LaB_6) using the precession electron diffraction tomography technique (PEDT).[40−42] The term 3D ED in this study refers to the precession electron diffraction tomography technique (PEDT). Data sets of non-oriented patterns were automatically recorded following the in-house fast-ADT procedure described in Plana-Ruiz et al.[43] with a precession device Nanomegas Digistar and a side-mounted CCD camera Olympus Veleta with a 14 bit dynamic range energy-dispersive analyzer Octane
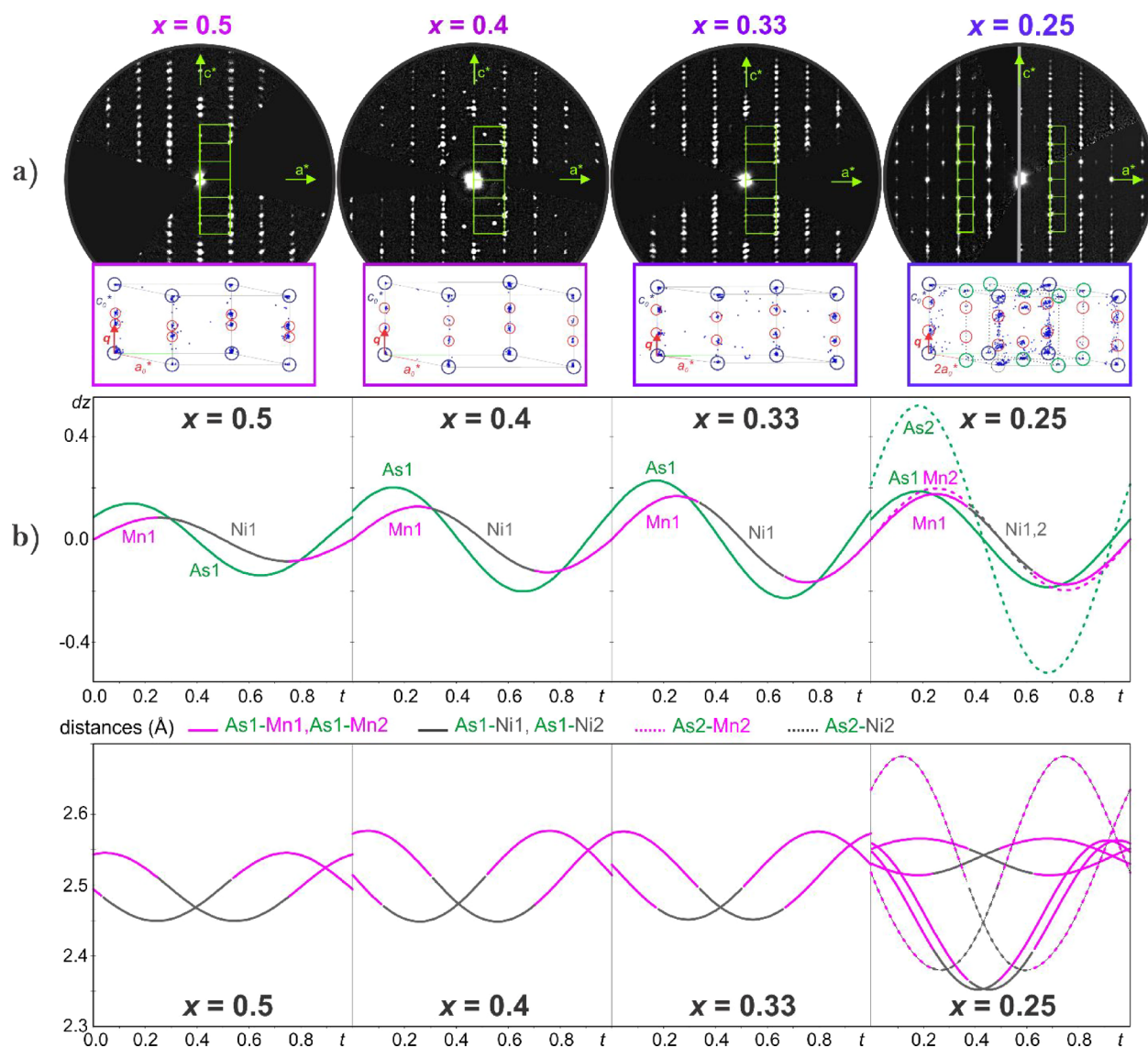
Figure 2. (a) Section *h0lm* for each composition *x* with the corresponding average modulated unit cell. For *x* = 0.25, the crystals show either a clear modulation associated with a weak doubling of the *a* parameter (right) or a strong doubling with more diffuse reflections (left). The reflections associated with the doubling of the *a* parameter are shown in green. In the unit cell inset, the main and satellite reflections are represented in blue and red, respectively. This section is built from two halves, from two different crystals: one where the modulation is more visible with sharper reflections (right half) and the second one where the doubling is more visible but with more diffuse features along *c** (left half). (b) On the top, displacement *dz* of the *z* coordinate due to modulation of the atoms As, Mn, and Ni for $Mn_{1-x}Ni_xAs$ samples with *x* = 0.50, 0.40, 0.33, and 0.25. Shown below are the corresponding As−Mn and As−Ni distance as a function of *t*.

silicon drift detector (SDD) EDAX. The precession semi-angle was set to 1°. 3D ED data reduction was performed using the computer program PETS2.[44] Data processing includes a correction of the misorientation of the frames (alpha and beta tilt, omega angle, coordinates of the center, etc.), scaling of the frames, and the fit of the intensity profile in order to improve the integration (for more information, see refs 44, 45). The result of the data reduction is an *hklm*-type file used in the structure solution and kinematical refinement. For the dynamical refinement, the data reduction produces an *hklm*-type files where each ED frame is considered independent.[46,47] Crystallographic details are given in Table 1. The structures for *x* = 0.50, *x* = 0.40, and *x* = 0.33 were directly refined using the model reported in Gonano et al.[37] For *x* = 0.25, the structure was solved using Superflip[48,49] in Jana2006[50] and refined using DYNGO in Jana2006. Note that the structure for *x* = 0.40 is already reported, but to ensure a better comparison, the crystal *x* = 0.40 was measured again in the same condition than the others.

2.3.1. *Refinements Parameters.* For *x* = 0.50, the refinement leads to $R(obs)/wR(obs)$ = 8.82%/9.96% for 1420/2341 observed/all reflections (771/810 main reflections with $R(obs)/wR(obs)_{main}$ = 7.10%/9.29%; 1420/2341 first order with $R(obs)/wR(obs)_{satellite1}$ = 15.12%/16.05%). For *x* = 0.33, it gives $R(obs)/wR(obs)$ = 11.06%/13.14% for 1441/2008 observed/all reflections (Nobs/all(main) = 637/674 with $R(obs)/wR(obs)_{main}$ = 9.74%/13.01%; Nobs/all-(order1) = 804/1334 with $R(obs)/wR(obs)_{order1}$ = 13.29%/13.44%) and for *x* = 0.25: $R(obs)/wR(obs)$ = 13.06%/13.97% for 1538/7015 observed/all reflections (Nobs/all(main) = 715/2316 with $R(obs)/wR(obs)_{main}$ = 9.93%/11.93%; Nobs/all(order1) = 823/4699 with $R(obs)/wR(obs)_{order1}$ = 18.40%/18.60%). The difference potential maps for all compositions are given in the Supporting Information.

2.4. Neutron Diffraction. Neutron powder diffraction (NPD) data were collected at room temperature on D1B, ILL, France, using wavelength λ = 2.52 Å. About 5 g of the sample was put into a cylindrical vanadium can. Rietveld refinements were carried out in JANA2006.[50] NPD was also collected at the NIMROD instrument at

ISIS pulsed neutron and muon source, UK.[51] Approximately 5 g of the sample was loaded into vanadium cans, and data was collected between 10 and 300 K.

2.5. X-ray Magnetic Circular Dichroism. XAS and XMCD spectra at the $L_{2,3}$ edges of Mn and Ni were measured at the DEIMOS beamline of the SOLEIL synchrotron (Synchrotron Radiation Facility, Gif-sur-Yvette, France). The end station is equipped with a cryomagnet providing a field of ± 7 T along the beam direction. The samples were cooled down at 5 K, and the absorption spectra were recorded in a total electron yield (TEY) mode. The XMCD signal was obtained by reversing both the helicity of the incoming X-ray and the direction of the magnetic field (± 6 T).

3. RESULTS AND DISCUSSION

We initiated our study of $Mn_{1-x}Ni_xAs$ samples ($x = 0.25$, 0.33, 0.40, and 0.50; average structure $P6_3/mmc$) in the super-structure range reported by Fjellvåg et al.[52] by high-angle annular dark field (HAADF) imaging, allowing good elemental contrasts for Mn and Ni. The experimental [110] and [100]-oriented images are presented in Figure 1. They reveal the presence of darker and brighter layers, which we associate with MnAs and NiAs slabs, perpendicular to the [001] direction. This statement is supported by an energy-dispersive X-ray spectroscopy mapping (EDX) shown in Figure 1d. Based on this interpretation, it is now evident that $x = 0.25$, 0.33, and 0.50 exhibit the same modulation phenomenon recently observed in $Mn_{0.60}Ni_{0.40}As$.[37] Meticulous image analysis performed on the images reveals a thickness variation of the different layers depending on the composition (x). The highest Ni-substituted sample $Mn_{0.50}Ni_{0.50}As$ shows an alternation of 2−3 octahedra thickness for both MnAs and NiAs layers, while the lowest Ni content, $Mn_{0.75}Ni_{0.25}As$, consists of 6−5/1−2 octahedra of MnAs/NiAs, respectively. Intermediate thicknesses, 3−4(MnAs)/2−3(NiAs) and 4−5(MnAs)/2−3(NiAs) are observed for $Mn_{0.60}Ni_{0.40}As$ and $Mn_{0.67}Ni_{0.33}As$, respectively. These results clearly indicate that we can tune the MnAs and NiAs layer thicknesses by controlling the composition. It should be noted that some stacking defects are observed on the top and bottom part of the $Mn_{0.75}Ni_{0.25}As$ [100] image (Figure 1d), and they appear to be scarce and not a representative of the general microscopic aspect of the observed crystallites.

To describe the MnAs−NiAs ordering phenomena evidenced as compositional modulations by means of HAADF and EDX analysis, we used the superspace formalism to analyze 3D ED data for $x = 0.50$, 0.40, 0.33, and 0.25 (Tables 1−3, Supporting Information). The 3D ED data for $x = 0.50$ and $x = 0.33$ show a similar feature as $Mn_{0.60}Ni_{0.40}As$ ($x = 0.40$) with the presence of first-order satellite reflections along c^* visible on the sections $h0lm$ (Figure 2a). Their reciprocal space is indexed in a modulated hexagonal cell and a modulation vector $q = \gamma c^*$ as reported for $x = 0.40$ ($\gamma = 0.366(2)$) with $\gamma(x = 0.50) = 0.418(1)$ and $\gamma(x = 0.33) = 0.322(4)$. The lattice parameters derived from 3D ED data and NPD data are given for all compositions in Table 2 (Supporting Information). For $x = 0.25$, the 3D ED data show in addition to the modulation along c^*, a doubling of the lattice parameter a_0. Thus, $Mn_{0.75}Ni_{0.25}As$ can be indexed in a modulated hexagonal unit cell with $a = 2a_0$, c_0 and $\gamma = 0.270(2)$ c^*. Our 3D ED experiments show that the $2a_0$ doubling can be observed with very weak intensity in some crystals with $x = 0.33$. The reciprocal space is for all samples described by the superspace group $P6_3/mmc(00\gamma)0000$ with condition $l = 2n$ on $hhlm$ (Figure 2a). The model reported for $Mn_{0.60}Ni_{0.40}As$ was properly adjusted,[37] and the respective 3D ED data were excellently refined in line with the dynamical theory of diffraction.[46,47,53]

In this model, Ni and Mn share the same atomic site and their ordering is described with a discontinuous crenel-like function using Δ, the width of the crenel along x_4 and x_4^0, the center of the crenel. The width of the atomic domain is defined as a function of x following $\Delta(Ni1) = x$ ($\Delta(Mn1) = 1 - x$) (Table 3 (Supporting Information)). The As site is described with one harmonic function that basically allows the atom to move from its average position along c. For $Mn_{0.75}Ni_{0.25}As$, the structure contains 2 Mn/Ni and As sites due to the cell doubling along a_0. A harmonic function is used to model the two As sites (As1 and As2). No restriction is applied on the models for the refinement and anisotropic displacement parameters are refined for $x = 0.50$, 0.40, and 0.33.

The refinement parameters are given in the Supporting Information (Table 1 and Section 2) and the structural parameters are presented in Table 3 (Supporting Information). Higher R factors are obtained for the satellite reflections because of their weaker intensities. This is even more pronounced for the very weak reflections $h = 2n + 1$ ($R(obs) = 30.21\%$) connected with the doubling of the a axis for $Mn_{0.75}Ni_{0.25}As$ ($x = 0.25$). The modulated structure and the values of the lattice parameters deduced from single-crystal 3D ED data are confirmed to fit the bulk situation as evaluated by Rietveld refinement of NPD data for all compositions (Figure 1e, Figure 2 (Supporting Information), and Table 4 (Supporting Information)). Note that the unindexed satellite peaks previously detected[52] fit well with the actual incommensurable model.

The modulation vector varies linearly with composition x (Figure 1f), confirmed from 3D ED data and Rietveld refinement of NPD (Table 4 (Supporting Information)). The structural models extracted from 3D ED refinements have been inserted in their corresponding HAADF image (Figure 1). At the average level, $Mn_{1-x}Ni_xAs$ can be described as a solid solution for $0.25 \leq x \leq 0.50$. However, at the microscopic level, the solid solution represents a very unusual and tunable nanostructure. Clearly, the modulation governs stacking sequences of MnAs and NiAs layers, as well as variations in their thicknesses along c (Figure 1). From $x = 0.50$ to $x = 0.25$, the amplitude of the positional modulation for Mn, Ni, and especially As increases gradually (Figure 2b). This is illustrated by more pronounced fluctuations of the Mn−As and Ni−As distances around the average value at higher Mn contents. The modulation amplitude of As is more pronounced than that of Mn/Ni, showing that As adapts most easily to the changes of the atomic environment. The doubling of the a parameter for $x = 0.25$ does not influence the stacking (nanostructure), but it allows two As environments, thus a higher degree of distortions of the coordination polyhedra around Mn and Ni. Due to the increased distortion, we believe that the composition $x = 0.25$ is close to the lower limit of Ni content for the modulated phase. This is also illustrated by the experimental HAADF imaging and the ED data by showing more disordered crystals with stacking faults as characterized by diffuse scattering along c (see top sections Figure 2a and Figure 1d).

The macroscopic magnetic properties of the $Mn_{1-x}Ni_xAs$ system were investigated in refs 52, 54. From temperature-dependent NPD and bulk magnetic measurements on $0.30 \leq x \leq 0.50$ compounds, an antiferromagnetic order was proposed as a magnetic ground state. Further, magnetization versus
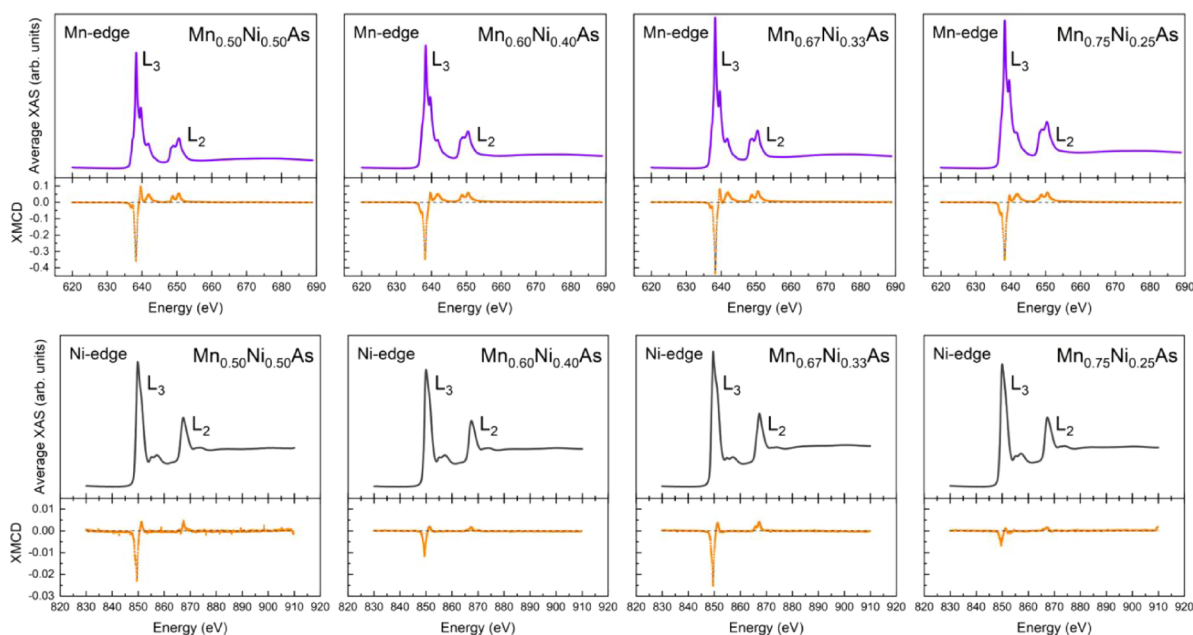
Figure 3. Average XAS and XMCD spectra of Mn (top) and Ni (bottom) for $Mn_{0.50}Ni_{0.50}As$, $Mn_{0.60}Ni_{0.40}As$, $Mn_{0.67}Ni_{0.33}As$, and $Mn_{0.75}Ni_{0.25}As$ at 5 K.

temperature measurements indicated magnetic ordering temperatures decreasing from ~190 to ~150 K with increasing x.[52] While the magnetic ground state would deserve to be revaluated to account for the nanoscale layering, we currently took advantage of the possibility to induce a finite magnetization at high fields to get a first insight into the magnetism of individual MnAs and NiAs layers. For that purpose, the element-selective and orbital-specific X-ray magnetic circular dichroism (XMCD) technique is used at the Mn $L_{3,2}$ and Ni $L_{3,2}$ edges ($2p \rightarrow 3d$) to determine the $3d$ magnetic moments of MnAs and NiAs layers, individually.

X-ray absorption spectroscopy (XAS) and XMCD spectra were collected at the Mn and Ni L-edges using total electron yield mode at 5 K in a ±6 T magnetic field (Figure 3), i.e., below the magnetic ordering temperatures. First, we observe that the XAS spectra of Mn and Ni for the layered compositions display the same features as the binary arsenides MnAs and NiAs (see Figure 3 (Supporting Information)) and that the absorption maxima are positioned at the same energy. For the MnAs and $Mn_{1-x}Ni_xAs$ samples, the Mn $L_{3,2}$ edges present a developed multiplet structure, with absorption maxima located at about 638.3 and 650.5 eV for the L_3 and L_2 edges, respectively, and several satellites peaks both below and above the L_3 maximum, as well as 1.5 and 2.2 eV below the maxima of the L_2 peak. In contrast, the Ni $L_{3,2}$ edges of the binary and ternary samples present a broader metallic-like spectral shape with absorption maxima at about 849.6 and 867.4 eV for the L_3 and L_2 edges, respectively. A double peak satellite is observed at 5.4 and 6.6 eV above the L_3 edge, and a weaker satellite is observed 6.5 eV above the L_2 edge. The spectral similarities between ternary and binary samples indicate that the electronic structures are comparable.

Clear XMCD signals are observed at the Mn and Ni edges, yet they exhibit a large difference in magnitude, the signal for Mn being one order of magnitude stronger than that of Ni. Similar to the XAS observations, the Mn and Ni XMCD spectral shapes do not evolve significantly along the $Mn_{1-x}Ni_xAs$ series. Spin and orbital moments were calculated

using magneto-optical sum rules[55] while assuming a $4s^2 3d^5$ and $4s^2 3d^8$ configuration for Mn(0) and Ni(0), respectively, the energy positions of the XAS maxima being found significantly lower in energy than those for Mn(III) references,[56] so consider that a metallic electronic configuration is a sound first approximation. We also neglect the magnetic dipole operator for both Mn and Ni ($\langle T_z \rangle = 0$), and the derived moments are presented in Table 1.

Table 1. Spin (μ_{spin}) and Orbital (μ_{orb}) Magnetic Moments Derived from XMCD Measurements for Mn $\langle 2a \rangle$ and Ni $\langle 2a \rangle$ in $Mn_{1-x}Ni_xAs$ ($0.25 \leq x \leq 0.50$) at $T = 5$ K and $B = 6$ T^a

composition	atom	μ_{spin} (μ_B/atom)	μ_{orb} (μ_B/atom)	$\mu_{spin} + \mu_{orb}$ (μ_B/atom)	M_{XMCD} (μ_B/f.u.)
$Mn_{0.50}Ni_{0.50}As$	Mn	0.28	$<-10^{-2}$	0.28	0.17
	Ni	0.03	0.02	0.05	
$Mn_{0.60}Ni_{0.40}As$	Mn	0.34	$<-10^{-2}$	0.34	0.22
	Ni	0.03	0.01	0.04	
$Mn_{0.67}Ni_{0.33}As$	Mn	0.32	-0.01	0.31	0.22
	Ni	0.03	0.01	0.04	
$Mn_{0.75}Ni_{0.25}As$	Mn	0.30	$<-10^{-2}$	0.30	0.23
	Ni	0.02	0.01	0.03	

$^a M_{XMCD}$ represents the total magnetization per sample.

First, let us note that the magnetizations derived from XMCD experiments are in overall quantitative agreement with that obtained from bulk magnetization versus field measurements (see a representative illustration for $x = 0.40$ in Figure 4 (Supporting Information)) where $M_{bulk}(6 \text{ T}) \approx 0.18$ μ_B/f.u. is reasonably in line with the 0.22 μ_B/f.u. obtained from XMCD). Then, consistent with the shape and amplitude of their respective XMCD spectra, the net Mn and Ni magnetic moments are oriented parallel to the applied magnetic field, but Mn moments are considerably larger than those of Ni. It is interesting to note that, in the range $0.25 \leq x \leq 0.50$, the elemental magnetic moments on Mn and Ni appear relatively

insensitive to Mn−Ni alloying, which is consistent with the segregation into MnAs and NiAs nanolayers.

The low Ni magnetization determined from XMCD measurements could be ascribed to a reminiscence of the Pauli paramagnetism of the NiAs parent compound. In contrast, the Mn layer achieves a large magnetization reminiscing the ferromagnetism of MnAs. As expected for a $3d^5$ configuration, the Mn orbital moment appears nearly negligible; hence, the magnetization of $Mn_{1-x}Ni_xAs$ samples is dominated by the Mn spin moment. The magnetic hysteresis cycles from bulk magnetization and from XMCD have a magnitude and overall shape resembling an antiferromagnet (Figure 4 (Supporting Information)), yet the curves deviate from linearity and the opening of a tiny hysteresis indicate that the order is not regularly antiferromagnetic. A long-periodicity helimagnetic order was observed in the genuine solid solution regime of $Mn_{1-x}Ni_xAs$ for $0.025 \leq x \leq 0.22$.[52] Possibly, a related ground state may persist at a higher Ni content although the materials segregated into MnAs−NiAs nanolayers.

To address the unresolved magnetic ordering, we employed NPD. Measurements at low temperatures with the D1B instrument (ILL, France) showed that it was not possible to resolve the magnetic ordering as it occurred at a too low scattering angle. The same is valid for the low temperature measurements presented in ref 52. We therefore turned to the NIMROD instrument (ISIS pulsed neutron and muon source, UK) with focus on accessing long d-spacing for $Mn_{1-x}Ni_xAs$ with $x = 0.50$, 0.40, and 0.33; $x = 0.25$ was not studied. At room temperature, the diffraction patterns display a strong peak from the structural modulation between 10 and 20 Å (Figure 5 (Supporting Information)), and we find the data to be in compliance with the structural models presented above. Upon cooling, a transition from the NiAs-type to MnP-type structure is evident by the appearance of the (101) reflection, which is allowed in the $Pnma$ space group and not in $P6_3/mmc$. The peak appears at $Q \approx 1.62$ Å^{-1} ($d \approx 3.86$ Å), depending on the composition. Upon cooling, the peak appears at 167 and 234 K for $x = 0.40$ and 0.33. The $x = 0.5$ ($Mn_{0.5}Ni_{0.5}As$) appears to remain hexagonal upon cooling. We note that the data gives information about the average structure, and to understand how the structural transition occurs within the individual MnAs and NiAs layers, local probes such as total scattering must be utilized.

From temperature-dependent NPD data, the magnetic ordering occurs at 154, 175, and 190 K for $x = 0.50$, 0.40, and 0.33 respectively. Below the magnetic ordering temperature, we observe new reflections from magnetic ordering (Figure 4). Significantly, the peaks appear at very long d-spacings, 30−70 Å. This suggests that the magnetic d-spacings are not commensurate with the unit cell nor with the modulation. Such long-range magnetic ordering is only compatible with incommensurate magnetic ordering, and we conclude that the system is either helimagnetic or display a spin density wave. We further find the helimagnetic state to be more likely based on the behavior of the system at a lower x.[52] It is however found that indexing of the periodicity based on a modulation along a^*, b^*, or c^* of the MnP-type structure is not possible. Correspondingly, single-crystal neutron diffraction of $Mn_{1-x}Ni_xAs$ is required for an accurate determination of the magnetic structure and is left for future work. These experiments will also be an option to rule out the possibility of
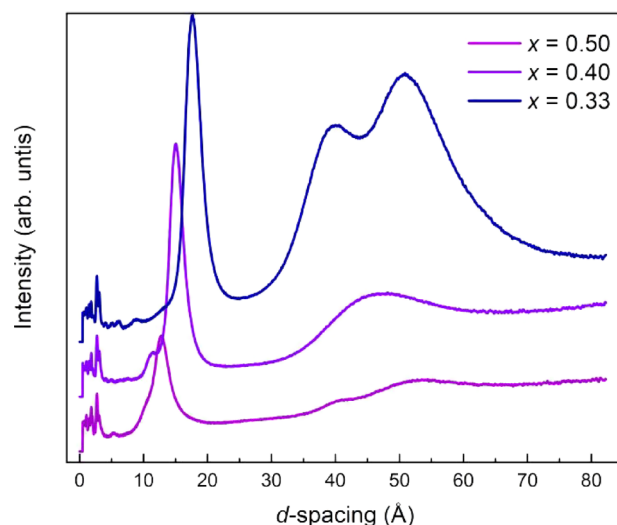
Figure 4. Neutron powder diffraction measured at 10 K of for $Mn_{1-x}Ni_xAs$ with $x = 0.50$, 0.40, and 0.33 collected at the NIMROD instrument at ISIS pulsed neutron and muon source, UK. The peaks between 10 and 20 Å originate from the occupational modulation, and the peaks between 30 and 70 Å appear upon cooling and originate from magnetic ordering.

an amplitude modulation of the magnetic moments, such as the one observed in spin density waves.

Bridging XMCD and NPD, we expect Mn to carry the magnetic moment, and the long periodicity indicates that ferromagnetic and antiferromagnetic interactions are competing. The competing interactions further indicate a delicate energy landscape between the different magnetic spin states/ orders, and it is therefore possible that the magnetic behavior of MnAs in the nanolayers contrasts to the ferromagnetic ordering of bulk MnAs due to small differences in cell parameters. The $Mn_{1-x}Ni_xAs$ system is therefore at the verge of a ferromagnetic state, and chemical tuning emerges as a possible route to further tune the magnetic properties of the materials presented here.

The closest parallel we can identify to the $Mn_{1-x}Ni_xAs$ ($0.25 \leq x \leq 0.50$) system is intergrowth in hematite−ilmenite minerals,[17,36] where extraordinary magnetic properties and huge exchange bias emerge from charge compensated nanolayers of basically antiferromagnetic character. However, such oxide minerals exhibit high electrical resistivity and are formed within geological timeframes, while the present segregation of a high moment MnAs layer with low moment NiAs is achieved in a metallic system during annealing for hours.

4. CONCLUSIONS

An extraordinary feature of $Mn_{1-x}Ni_xAs$ is the unique layering and strong interlayer bonding that can be controlled at the atomic scale, similar to a consecutive growth of thin film layers, but with a unique precision as the periodicity is inherent to the system, and with an average periodicity that can be tuned by means of the Mn:Ni composition, x. We present in Figure 5 an overview of the nanolayered system with a focus on the variation of the MnAs−NiAs nanolayers. The strength of magnetization is indicated for the different types of layers. Further studies on the physical properties of the $Mn_{1-x}Ni_xAs$ ($0.25 \leq x \leq 0.50$) system are highly desirable regarding the rich physics and exotic phenomena that can be expected as a
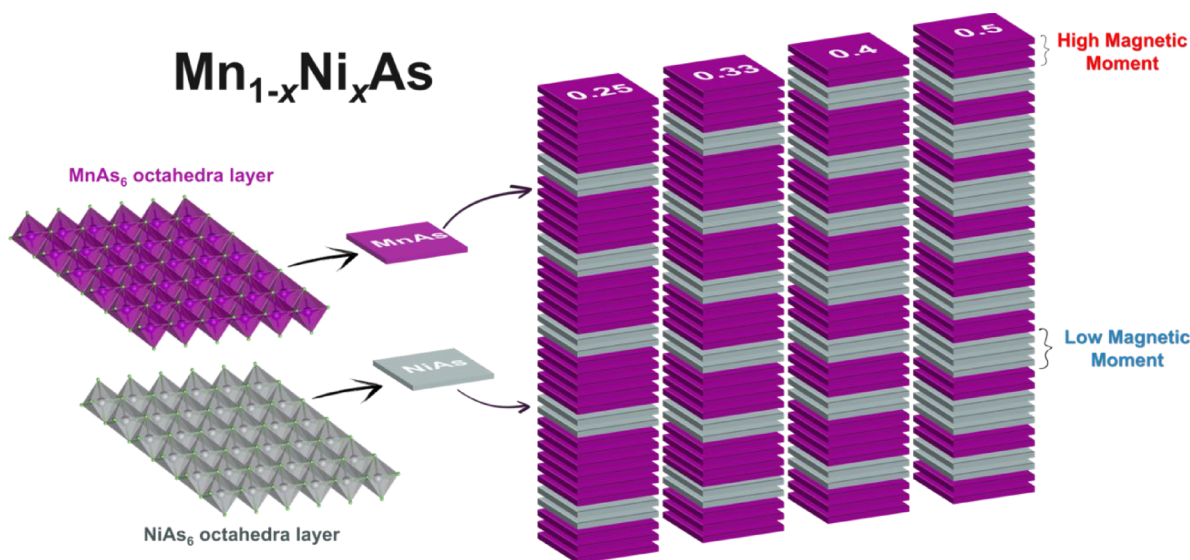
Figure 5. Illustration of the variation of the layering phenomenon depending on the composition with MnAs layers with a high magnetic moment and NiAs layers with a low magnetic moment.

result of this nanoscale layering. The $Mn_{1-x}Ni_xAs$ system may open a path to a new class of materials with layers of high and low magnetization with potential applications within spintronics.

ASSOCIATED CONTENT

Ⓢ Supporting Information

The Supporting Information is available free of charge at https://pubs.acs.org/doi/10.1021/acs.chemmater.1c00760.

Electron diffraction patterns, neutron diffraction refinements, XAS spectra, magnetization measurements, potential maps, and tables of refinements parameters (PDF)

AUTHOR INFORMATION

Corresponding Authors

Bruno Gonano − *Center for Materials Science and Nanotechnology, Department of Chemistry, University of Oslo, N-0315 Oslo, Norway;* ⓘ orcid.org/0000-0002-7331-2131; Email: b.r.g.gonano@smn.uio.no

Helmer Fjellvåg − *Center for Materials Science and Nanotechnology, Department of Chemistry, University of Oslo, N-0315 Oslo, Norway;* Email: helmer.fjellvag@kjemi.uio.no

Authors

Øystein Slagtern Fjellvåg − *Department for Hydrogen Technology, Institute for Energy Technology, NO-2027 Kjeller, Norway;* ⓘ orcid.org/0000-0003-0215-5260

Gwladys Steciuk − *Institute of Physics, Academy of Sciences of the Czech Republic, Prague 18221, Czech Republic*

Francois Guillou − *College of Physics and Electronic Information, Inner Mongolia Normal University, 010022 Hohhot, China*

Dipankar Saha − *Center for Materials Science and Nanotechnology, Department of Chemistry, University of Oslo, N-0315 Oslo, Norway;* ⓘ orcid.org/0000-0002-2197-2568

Denis Pelloquin − *Laboratoire CRISMAT, UMR 6508 CNRS ENSICAEN, 14050 Caen, France;* ⓘ orcid.org/0000-0001-8381-9318

Complete contact information is available at:
https://pubs.acs.org/10.1021/acs.chemmater.1c00760

Author Contributions

B.G., Ø.S.F., and H.F. designed and directed the study. B.G. and D.S. synthesized the samples. B.G. and D.P. performed STEM experiments and analysis. G.S. conducted and analyzed 3D ED. B.G., Ø.S.F., and D.S. conducted the NPD experiments, and G.S. contributed to the analysis. B.G., Ø.S.F., and D.S. conducted the XMCD experiments, and B.G. and F.G. performed the analysis. B.G. and Ø.S.F. wrote the manuscript with contributions from all co-authors.

Notes

The authors declare no competing financial interest.

ACKNOWLEDGMENTS

■ REFERENCES

(1) Roy Chowdhury, R.; Dhara, S.; Das, I.; Bandyopadhyay, B.; Rawat, R. Large Positive Magnetoresistance in Intermetallic Compound $NdCo_2Si_2$. *J. Magn. Magn. Mater.* **2018**, *451*, 625−628.

(2) Lee, Y.; Liu, Z. Q.; Heron, J. T.; Clarkson, J. D.; Hong, J.; Ko, C.; Biegalski, M. D.; Aschauer, U.; Hsu, S. L.; Nowakowski, M. E.; Wu, J.; Christen, H. M.; Salahuddin, S.; Bokor, J. B.; Spaldin, N. A.; Schlom, D. G.; Ramesh, R. Large Resistivity Modulation in Mixed-Phase Metallic Systems. *Nat. Commun.* **2015**, *6*, 5959.

(3) Kamishima, K.; Goto, T.; Nakagawa, H.; Miura, N.; Ohashi, M.; Mori, N.; Sasaki, T.; Kanomata, T. Giant Magnetoresistance in the Intermetallic Compound Mn_3GaC. *Phys. Rev. B* **2001**, *63*, No. 024426.

(4) Balli, M.; Jandl, S.; Fournier, P.; Kedous-Lebouc, A. Advanced Materials for Magnetic Cooling: Fundamentals and Practical Aspects. *Appl. Phys. Rev.* **2017**, *4*, No. 021305.

(5) Gupta, S.; Suresh, K. G. Review on Magnetic and Related Properties of RTX Compounds. *J. Alloys Compd.* **2015**, *618*, 562−606.

(6) Fujita, A.; Fujieda, S.; Hasegawa, Y.; Fukamichi, K. Itinerant-Electron Metamagnetic Transition and Large Magnetocaloric Effects in $La(Fe_xSi_{1-x})_{(13)}$ Compounds and Their Hydrides. *Phys. Rev. B* **2003**, *67*, 104416.

(7) Gschneidner, K. A., Jr.; Pecharsky, V. K.; Tsokol, A. O. Recent Developments in Magnetocaloric Materials. *Rep. Prog. Phys.* **2005**, *68*, 1479−1539.

(8) Krenke, T.; Duman, E.; Acet, M.; Wassermann, E. F.; Moya, X.; Mañosa, L.; Planes, A. Inverse Magnetocaloric Effect in Ferromagnetic Ni-Mn-Sn Alloys. *Nat. Mater.* **2005**, *4*, 450−454.

(9) Buďko, S. L.; Lapertot, G.; Petrovic, C.; Cunningham, C. E.; Anderson, N.; Canfield, P. C. Boron Isotope Effect in Superconducting MgB_2. *Phys. Rev. Lett.* **2001**, *86*, 1877−1880.

(10) Cava, R. J.; Takagi, H.; Zandbergen, H. W.; Krajewski, J. J.; Peck, W. F., Jr.; Siegrist, T.; Batlogg, B.; van Dover, R. B.; Felder, R. J.; Mizuhashi, K.; Lee, J. O.; Eisaki, H.; Uchida, S. Superconductivity in the Quaternary Intermetallic Compounds $LnNi_2B_2C$. *Nature* **1994**, *367*, 252−253.

(11) Robinson, D. W. *Magnetism and the Chemical Bond*. John B. Goodenough. Interscience Wiley; New York, *Science* **1964**, *143* (3601), 33−34, DOI: 10.1126/science.143.3601.33-a.

(12) Lévy, F. *Crystallography and Crystal Chemistry of Materials with Layered Structures*. Springer Netherlands, Dordrecht, 1976, 1−50, DOI: 10.1007/978-94-010-1433-5

(13) Brown, S.; Grüner, G. Charge and Spin Density Waves. *Scientific American* **1994**, *270*, 50−56.

(14) Overhauser, A. Spin Density Waves in an Electron Gas. *Phys. Rev.* **1962**, *128*, 1437.

(15) Peierls, R. E. *Quantum Theory of Solids*; Clarendon Press, Oxford, 1955, 1−229

(16) Makhfudz, I.; Pujol, P. Hole Properties On and Off Magnetization Plateaus in 2-d Antiferromagnets. *Phys. Rev. Lett.* **2015**, *114*, No. 087204.

(17) McEnroe, S. A.; Carter-Stiglitz, B.; Harrison, R. J.; Robinson, P.; Fabian, K.; McCammon, C. Magnetic Exchange Bias of More than 1 Tesla in a Natural Mineral Intergrowth. *Nat. Nano.* **2007**, *2*, 631−634.

(18) Blatter, G.; Geshkenbein, V. B.; Larkin, A. I. From Isotropic to Anisotropic Superconductors: A Scaling Approach. *Phys. Rev. Lett.* **1992**, *68*, 875−878.

(19) Machida, K. Spin Density Wave and Superconductivity in Highly Anisotropic Materials. *J. Phys. Soc. Jpn.* **1981**, *50*, 2195−2202.

(20) Felser, C.; Fecher, G. H.; Balke, B. Spintronics: A Challenge for Materials Science and Solid-State Chemistry. *Am. Ethnol.* **2007**, *46*, 668−699.

(21) Jedema, F. J.; Filip, A. T.; van Wees, B. J. Electrical Spin Injection and Accumulation at Room Temperature in an All-Metal Mesoscopic Spin Valve. *Nature* **2001**, *410*, 345−348.

(22) Freitas, P. P.; Silva, F.; Oliveira, N. J.; Melo, L. V.; Costa, L.; Almeida, N. Spin Valve Sensors. *Sens. Actuators, A* **2000**, *81*, 2−8.

(23) Kools, J. C. S. Exchange-Biased Spin-Valves for Magnetic Storage. *IEEE Trans. Magn.* **1996**, *32*, 3165−3184.

(24) Milyaev, M.; Naumova, L.; Chernyshova, T.; Proglyado, V.; Kamensky, I.; Krinitsina, T.; Ryabukhina, M.; Ustinov, V. Magnetization Reversal and Inverted Magnetoresistance of Exchange-Biased Spin Valves with a Gadolinium Layer. *J. App. Phys.* **2017**, *121*, 123902.

(25) Gajek, M.; Bibes, M.; Fusil, S.; Bouzehouane, K.; Fontcuberta, J.; Barthélémy, A.; Fert, A. Tunnel Junctions with Multiferroic Barriers. *Nat. Mater.* **2007**, *6*, 296−302.

(26) Julliere, M. Tunneling between Ferromagnetic Films. *Phys. Lett. A* **1975**, *54*, 225−226.

(27) Nakano, T.; Oogane, M.; Furuichi, T.; Ando, Y. Magnetic Tunnel Junctions Using Perpendicularly Magnetized Synthetic Antiferromagnetic Reference Layer for Wide-Dynamic-Range Magnetic Sensors. *Appl. Phys. Lett.* **2017**, *110*, No. 012401.

(28) Rashba, E. I. Theory of Electrical Spin Injection: Tunnel Contacts as a Solution of the Conductivity Mismatch Problem. *Phys. Rev. B* **2000**, *62*, R16267−R16270.

(29) Sbiaa, R.; Meng, H.; Piramanayagam, S. N. Materials with Perpendicular Magnetic Anisotropy for Magnetic Random Access Memory. *Phys. Status Solidi RRL* **2011**, *5*, 413−419.

(30) Tudu, B.; Tiwari, A. Recent Developments in Perpendicular Magnetic Anisotropy Thin Films for Data Storage Applications. *Vacuum* **2017**, *146*, 329−341.

(31) Wetzig, K.; Schneider, C. M. *Metal Based Thin Films for Electronics*; John Wiley & Sons, 2006, 2−10

(32) Ohtsuki, T.; Chainani, A.; Eguchi, R.; Matsunami, M.; Takata, Y.; Taguchi, M.; Nishino, Y.; Tamasaku, K.; Yabashi, M.; Ishikawa, T.; Oura, M.; Senba, Y.; Ohashi, H.; Shin, S. Role of Ti 3d Carriers in Mediating the Ferromagnetism of $Co:TiO_2$ Anatase Thin Films. *Phys. Rev. Lett.* **2011**, *106*, No. 047602.

(33) Pratt, W. P. Perpendicular Giant Magnetoresistances of Ag/Co Multilayers. *Phys. Rev. Lett.* **1991**, *66*, 4.

(34) Johnson, M. Analysis of Anomalous Multilayer Magnetoresistance within the Thermomagnetoelectric System. *Phys. Rev. Lett.* **1991**, *67*, 3594−3597.

(35) Fraerman, A. A.; Shereshevskii, I. A. Magnetocaloric Effect in Ferromagnet/Paramagnet Multilayer Structures. *JETP Lett.* **2015**, *101*, 618−621.

(36) Robinson, P.; Harrison, R. J.; McEnroe, S. A.; Hargraves, R. B. Lamellar Magnetism in the Haematite−Ilmenite Series as an Explanation for Strong Remanent Magnetization. *Nature* **2002**, *418*, 517.

(37) Gonano, B.; Fjellvåg, Ø. S.; Steciuk, G.; Saha, D.; Pelloquin, D.; Fjellvåg, H. Exotic Compositional Ordering in Manganese−Nickel−Arsenic (Mn-Ni-As) Intermetallics. *Am. Ethnol.* **2020**, *59*, 22382−22387.

(38) Gemmi, M.; Lanza, A. E. 3D Electron Diffraction Techniques. *Acta Cryst B* **2019**, *75*, 495−504.

(39) Gemmi, M.; Mugnaioli, E.; Gorelik, T. E.; Kolb, U.; Palatinus, L.; Boullay, P.; Hovmöller, S.; Abrahams, J. 3D Electron Diffraction: the nanocrystallography revolution. *ASC Cent. Sci.* **2019**, *5*, 1315−1329.

(40) Vincent, R.; Midgley, P. A. Double Conical Beam-Rocking System for Measurement of Integrated Electron Diffraction Intensities. *Ultramicroscopy* **1994**, *53*, 271−282.

(41) Kolb, U.; Gorelik, T.; Otten, M. T. Towards Automated Diffraction Tomography. Part II–Cell Parameter Determination. *Ultramicroscopy* **2008**, *108*, 763−772.

(42) Mugnaioli, E.; Gorelik, T.; Kolb, U. "Ab Initio" Structure Solution from Electron Diffraction Data Obtained by a Combination of Automated Diffraction Tomography and Precession Technique. *Ultramicroscopy* **2009**, *109*, 758−765.

(43) Plana-Ruiz, S.; Krysiak, Y.; Portillo, J.; Alig, E.; Estradé, S.; Peiró, F.; Kolb, U. Fast-ADT: A Fast and Automated Electron Diffraction Tomography Setup for Structure Determination and Refinement. *Ultramicroscopy* **2020**, *211*, 112951.

(44) Palatinus, L.; Brázda, P.; Jelínek, M.; Hrdá, J.; Steciuk, G.; Klementová, M. Specifics of the Data Processing of Precession

Electron Diffraction Tomography Data and Their Implementation in the Program PETS2.0. *Acta Crystallographica Section B: Structural Science, Crystal Engineering and Materials* **2019**, *75*, 512−522.

(45) Palatinus, L.; Petříček, V.; Correâ, C. A. Structure Refinement Using Precession Electron Diffraction Tomography and Dynamical Diffraction: Theory and Implementation. *Acta Crystallographica Section A: Foundations and Advances* **2015**, *71*, 235−244.

(46) Brázda, P.; Palatinus, L.; Babor, M. Electron Diffraction Determines Molecular Absolute Configuration in a Pharmaceutical Nanocrystal. *Science* **2019**, *364*, 667−669.

(47) Palatinus, L.; Corrêa, C. A.; Steciuk, G.; Jacob, D.; Roussel, P.; Boullay, P.; Klementová, M.; Gemmi, M.; Kopeček, J.; Domeneghetti, M. C.; Cámara, F.; Petříček, V. Structure Refinement Using Precession Electron Diffraction Tomography and Dynamical Diffraction: Tests on Experimental Data. *Acta Crystallographica Section B Structural Science, Crystal Engineering and Materials* **2015**, *71*, 740−751.

(48) Palatinus, L.; Chapuis, G. SUPERFLIP − a Computer Program for the Solution of Crystal Structures by Charge Flipping in Arbitrary Dimensions. *J. Appl. Crystallogr.* **2007**, *40*, 786−790.

(49) Palatinus, L. The Charge-Flipping Algorithm in Crystallography. *Acta Cryst B, Acta Cryst Sect B, Acta Crystallogr B, Acta Crystallogr Sect B, Acta Crystallogr B Struct Crystallogr Cryst Chem, Acta Crystallogr Sect B Struct Crystallogr Cryst Chem* **2013**, *69*, 1−16.

(50) Petrícek, V.; Dušek, M.; Palatinus, L. Crystallographic Computing System JANA2006: General Features. *Zeitschrift fur Kristallographie* **2014**, *229*, 345−352.

(51) Bowron, D. T.; Soper, A. K.; Jones, K.; Ansell, S.; Birch, S.; Norris, J.; Perrott, L.; Riedel, D.; Rhodes, N. J.; Wakefield, S. R.; Botti, A.; Ricci, M.-A.; Grazzi, F.; Zoppi, M. NIMROD: The Near and InterMediate Range Order Diffractometer of the ISIS Second Target Station. *Rev. Sci. Instrum.* **2010**, *81*, No. 033905.

(52) Fjellvag, H.; Kjekshus, A.; Andresen, A.; Zieba, A. Structural and Magnetic-Properties of $Mn_{1-t}Ni_tAs$. *J. Magn. Magn. Mater.* **1986**, *61*, 61−80.

(53) Steciuk, G.; Palatinus, L.; Rohlíček, J.; Ouhenia, S.; Chateigner, D. Stacking Sequence Variations in Vaterite Resolved by Precession Electron Diffraction Tomography Using a Unified Superspace Model. *Sci. Rep.* **2019**, *9*, 1−12.

(54) Delphin, I.; Selte, K.; Kjekshus, A.; Andresen, A. Structural and Magnetic-Properties of $Cr_{1-t}Ni_tAs$, $Mn_{1-t}Ni_tAs$, and $Fe_{1-t}Ni_tAs$. *Acta Chemica Scandinavica Series a-Physical and Inorganic Chemistry* **1978**, *32*, 179−185.

(55) Chen, C. T.; Idzerda, Y. U.; Lin, H.-J.; Smith, N. V.; Meigs, G.; Chaban, E.; Ho, G. H.; Pellegrin, E.; Sette, F. Experimental Confirmation of the X-Ray Magnetic Circular Dichroism Sum Rules for Iron and Cobalt. *Phys. Rev. Lett.* **1995**, *75*, 152−155.

(56) Gao, L.; Wang, X.; Ye, X.; Wang, W.; Liu, Z.; Qin, S.; Hu, Z.; Lin, H.-J.; Weng, S.-C.; Chen, C.-T.; Ohresser, P.; Baudelet, F.; Yu, R.; Jin, C.; Long, Y. Near-Room-Temperature Ferrimagnetic Ordering in a B-Site-Disordered 3d−5d-Hybridized Quadruple Perovskite Oxide, $CaCu_3Mn_2Os_2O_{12}$. *Inorg. Chem.* **2019**, *58*, 15529−15535.